arXiv:1405.3702v1 [cond-mat.mtrl-sci] 14 May 2014

Microscopic origin of pressure-induced isosymmetric transitions in fluoromanganate cryolites

Nenian Charles* and James M. Rondinelli†
Department of Materials Science & Engineering, Drexel University, Philadelphia, PA 19104, USA
(Dated: May 16, 2014)

Using first-principles density functional theory calculations, we investigate the hydrostatic pressure-induced reorientation of the Mn–F Jahn-Teller bond axis in the fluoride cryolite Na_3MnF_6. We find a first-order isosymmetric transition occurs between crystallographically equivalent monoclinic structures at approximately 2.15 GPa, consistent with earlier experimental studies. Analogous calculations for isostructural $3d^0$ Na_3ScF_6 show no evidence of a transition up to 6.82 GPa. Mode crystallography analyses of the pressure-dependent structures in the vicinity of the transition reveals a clear evolution of the Jahn-Teller bond distortions in cooperation with an asymmetrical stretching of the equatorial fluorine atoms in the MnF_6 octahedral units. We identify a change in orbital occupancy of the e_g manifold in the $3d^4$ Jahn-Teller active Mn(III) to be responsible for the transition, which stabilizes one monoclinic $P2_1/n$ variant over the other.

PACS numbers: 61.50.Ks, 74.62.Fj, 71.15.Mb

I. INTRODUCTION

Perovskite transition metal compounds with ABX_3 stoichiometry, where X is either oxygen or fluorine, have been extensively studied owing to their ability to support a rich set of physical phenomena ranging from multiferroisim to superconductivity.[1–4] Many of these properties are a direct consequence of electron-lattice interactions across structural phase transitions owing to symmetry reductions, which alter chemical bonding pathways and electronic properties through distortions and rotations of BX_6 octahedra. Indeed, the physical properties of perovskites can be tailored by changing the bonding environments by manipulating the BX_6 size, shape, and connectivity[5] using chemical pressure or epitaxial strain.[6–9] Thus, for electronic function engineering purposes it is useful to understand the tendency of a perovskite to distort, or undergo a structural transitions, which can be estimated using the Goldschmidt tolerance factor.[10]

The tremendous success of perovskites has sparked interest in a closely related set of materials, the $A_2BB'X_6$ double perovskites with multiple cations that order among various planes in a periodic fashion (Fig. 1). The additional compositional ordering degree of freedom not found in simple perovskites[11,12] can be used to obtain desirable ferroic responses,[13,14] and explore correlated electron properties.[15–17] It is important to note that while there are a multitude of studies on perovskites and double perovskites, *i.e.*, most of the materials physics literature is keenly focused on X=O transition metal oxides,[1] fluoride compounds, however, also show an affinity for functional electronic behavior, including mutiferroicity.[18–21]

For the case of rock salt ordered double perovskites with two possible B cations (B and B′) with X = F (fluorine), these compounds are generally referred to by one of the two prototypes illustrated in Fig. 1. The first class being *cryolite*, after the compound Na_3AlF_6.[22] This family contains compounds with [12]-coordinate A sites in the ideal structure, whereby the same cation on the A site is chemically identical to one at the octahedrally coordinated B site (A = B), while the B′ cation remains unique. This results in the stoichiometry $A_3B'F_6$ for cryolite. The other prototype is *elpasolite*, which is named for the mineral K_2NaAlF_6.[23] It also refers to structures with 12-fold coordinated A cations, but unlike cryolite, the two octahedrally coordinated B sites are chemically distinct species (B and B′).[24,25] Thus the stoichiometry for elpasolite is $A_2BB'F_6$.

Similar to the transition metal perovksite oxides, the ground state properties of cryolites and elpasolites (double

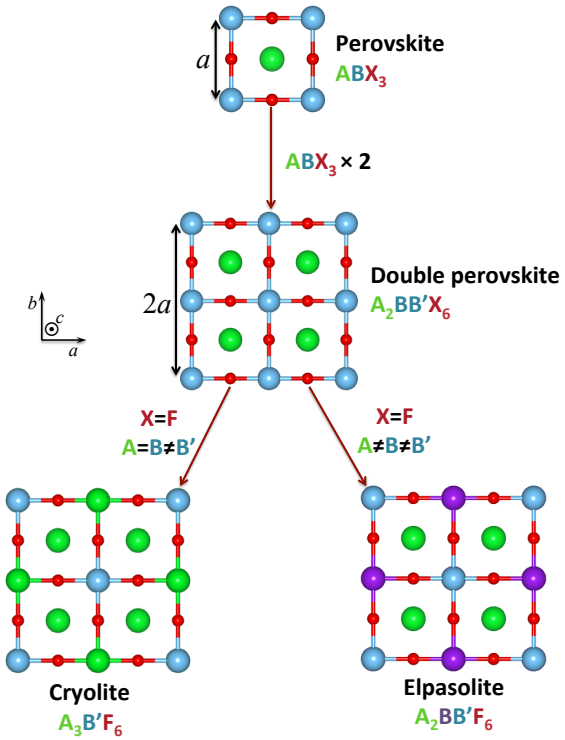

FIG. 1. Ideal structures of the double perovskite fluorides cryolite ($A_3B'F_6$, left) and elpasolite ($A_2BB'F_6$, right) as they relate to the cubic ABX_3 perovskite structure (top).

perovskite fluorides) are also strongly structure and symmetry dependent. The tendency for any double perovskite to distort is estimated using a generalized tolerance factor

$$t = \frac{\sqrt{2}(r_{\mathrm{A}} + r_{\mathrm{X}})}{(r_{\mathrm{B}} + r_{\mathrm{B}'} + 2r_{\mathrm{X}})},$$

where r_{A}, r_{B}, $r_{\mathrm{B}'}$, and r_{X} are the ionic radii of the different chemical species taking into account the appropriate coordination number and spin states approximated by the Shannon and Prewitt radii.[26,27] In the case of double perovskite fluoride compounds ($r_{\mathrm{X}} = r_{\mathrm{F}}$), the use of the Shannon radius for fluorine with a coordination number of 2 ($r_{\mathrm{F}} = 1.28.5$ Å) accurately reproduces observed B′–F bond lengths.[25] For tolerance factor values in the range $0.91 \leq t \leq 1.00$, the cryolite and elpasolites tend to remain cubic—a much larger cubic stability field than found in ABX_3 perovskites,[28] which are anticipated only to be cubic for $t = 1$. For the case where t<0.91, the double perovskite fluorides also have a stronger affinity for octahedral rotations, and for t>1.00, like the oxides, cryolite and elpasolite adopt hexagonal symmetries.[25]

Here we focus on the cryolite Na_3MnF_6 ($t = 0.89$), which possesses a strong first-order active Jahn-Teller d^4 Mn^{3+} cation and exhibits a distorted monoclinic $P2_1/n$ (space group no. 14) structure with both in-phase and out-of-phase MnF_6 octahedral rotations in its ground state (Fig. 2).[29] Interestingly, Na_3MnF_6 is reported to experimentally undergo an isostructural first-order monoclinc-to-monoclinic phase transition with hydrostatic pressure.[30] Such iso-structural/iso-symmetric phase transitions (IPT) transitions without symmetry reductions[31] are scientifically interesting, because they infrequently occur in inorganic condensed matter phases that are known to exhibit displacive transitions.[32] Microscopic origins for such transitions include spin-state transitions,[33] electronic or magnetic polarization rotation,[34] or from bond reconfigurations due to mechanical epitaxial strain constraints.[35–38] The IPT in Na_3MnF_6 is experimentally found to be reversible while showing characteristic first order hysteric behavior. Above and below the critical pressure value for the phase transition, the authors of Ref. 30 were able to identify both changes in the amplitude of the short and long Mn–F bond lengths and the relative orientation of these bond pairs with respect to the monoclinic axes. The atomic and electronic features responsible for the phase transition, however, remain unknown: is it due to spontaneous strain, the Mn electronic degrees of freedom, or strong electron–lattice interactions?

Herein, we use density functional theory calculations to identify the microscopic origin of the pressure-induced IPT in the fluoromanganate Na_3MnF_6. We find that the ground state monoclinic structure is stabilized through a combination of energy lowering MnF_6 octahedral rotations and Jahn-Teller (JT) bond elongations; the latter arise to remove the orbital degeneracy owing to electron occupation of the majority spin $e_g^{\uparrow}$-manifold presented by a cubic crystal field. These combined effects produce a crystal structure at ambient pressure that exhibits elongated Mn–F bonds along the long, crystallographic c axis depicted in Fig. 2(b), and is common for manganates with axial ratios $c/a > 1$.[39,40] Upon application of hydrostatic pressure in Na_3MnF_6, we find a reorientation of the long JT Mn–F bond occurs for unit cell volumes of 240 ± 0.1 Å^3, corresponding to an experimental pressure between 2.10 GPa and 2.15 GPa in agreement with Ref. 30. At the electronic structure level, we find that the low-pressure fluoromanganate phases have fully occupied $d_{z^2-r^2}$ orbitals, whereas in the high-pressure phase, the occupancy reverses and is predominately of $d_{x^2-y^2}$ orbital character. Furthermore, we find that the pressure renormalizes the mode stiffness of the Jahn-Teller distortion, which due to the electron-lattice coupling facilitates the electronic transition. Uncovering the microscopic origins of the iso-structural first order phase transition sheds light on the effect of stress on the magnetic, electronic and structural degrees of freedom in Na_3MnF_6. Thus, improving our understanding of electronic and structural transitions in bulk d^4 fluoromanganites, which may facilitate the design of IPTs in thin film geometries for future device applications.

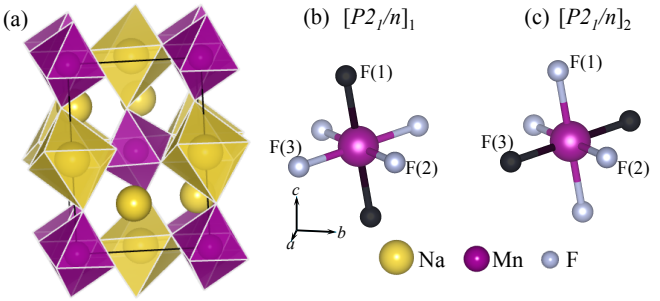

FIG. 2. Equilibrium zero kelvin structure of Na_3MnF_6, and the MnF_6 octahedra of the (b) low pressure $[P2_1/n]_1$ and (c) high pressure $[P2_1/n]_2$, phases. The long Mn–F bond axis, referred in the text as the Jahn-Teller (JT) bond axis, is highlighted in black and the ferrodistortive packing of these octahedra along the c-axis is the distinguishing structural feature across the monoclinic-to-monoclinic transition.

II. COMPUTATIONAL & SIMULATION DETAILS

We performed density functional theory calculations with the general gradient approximation (GGA) of Perdew-Burke-Ernzerhof revised for solids[41] (PBEsol) as implemented in the Vienna *Ab initio* Simulation Package (VASP)[42,43] with the projector augmented wave (PAW) method[44] to treat the core and valence electrons using the following valence configurations: $2p^6 3s^1$ for Na, $3p^6 4s^1 3d^6$ for Mn, and $2s^2 2p^5$ for F. We used a $7 \times 7 \times 7$ Monkhorst-Pack k-point mesh[45] with Gaussian smearing (0.1 eV width) for the Brillouin zone (BZ) integrations and a 600 eV plane wave cutoff. Spin-polarized structural relaxations were performed until the Hellmann-Feynman forces were less than 1 meV Å^{-1} for each atom position.

Magnetic Order. The long-range spin order for Na_3MnF_6 has not been previously reported. Therefore, prior to carrying out the pressure study, we explored the energetics for A-type antiferromagnetic order (in-plane ferromagnetic coupling between Mn sites, with out-of-plane antiferromagnetic coupling) and ferromagnetic order on the monoclinic $P2_1/n$ (ambient) structure with the JT Mn–F bond directed along the c axis. These two magnetic configurations are compatible with the 20 atom unit cell used in all calculations. From our total energy calculations of the fully relaxed phases, we find that the ferromagnetic configuration is essentially degenerate with the antiferromagnetic configuration: There is less than a 0.1% difference in cell volume and an energy difference of 0.4 meV per formula unit (f.u.). These small differences between the magnetic variants also persist for calculations performed at elevated pressures. Owing to the strong ionic character of the fluoride and the fact that there appears to be very weak spin–lattice coupling, we use structures with ferromagnetic (FM) order throughout to perform the hydrostatic pressure simulations. As described below, the FM order yields excellent agreement with experimental structural data.

Application of Hydrostatic Pressure. We computationally mimic the experimental hydrostatic pressure study by imposing the lattice constants and monoclinic angles reported in Ref. 30 while allowing the internal coordinates to fully relax to obtain the total energies for both the low-pressure ($[P2_1/n]_1$) and high-pressure ($[P2_1/n]_2$) phases. Throughout, we distinguish between the two phases by using the space group label with an additional index, 1 or 2, appended to the end to indicate if it is the low-pressure (phase 1) or high-pressure (phase 2) Na_3MnF_6 structure. The starting atomic configuration for the $[P2_1/n]_1$ phases employ the positions obtained from our fully relaxed zero pressure DFT-PBEsol simulations, whereas for the $[P2_1/n]_2$ structural relaxations, we initialize the atomic positions to those reported experimentally.[30]

III. RESULTS

A. Na_3MnF_6 Equilibrium Structure

Before performing the hydrostatic pressure study on Na_3MnF_6, we first determine the equilibrium structure at zero pressure with ferromagntic spin order. Consistent with experiments, we find a distorted monoclinic structure with in-phase MnF_6 octahedral rotations about the c axis and out-of-phase tilts. The combination of rotations and tilts gives the $a^-a^-c^+$ tilt pattern as described within Glazer notation.[46] Table I shows that the PBEsol functional provides an accurate description of the structural parameters of Na_3MnF_6 when compared to experiment. The error in the cell volume is ∼0.05%, under the constraint that the PBEsol structure has the same monoclinic angle as that reported in Ref. 29.

TABLE I. Comparison between the internal coordinates given in reduced units and lattice parameters a, b, and c (Å) for monoclinic Na_3MnF_6 ($P2_1/n$) obtained from DFT-PBEsol calculations and x-ray synchrotron experiments.[29] The monoclinic angle, $\beta = 88.96°$, is constrained to the experimental value. The unit cell volumes obtained from DFT and experiment are 251.09 and 250.97 Å^3, respectively. The Mn and Na(1) cations occupy the Wyckoff positions (WP) $2a\,(0,0,0)$ and $2b\,(0,0,1/2)$, respectively without free parameters, while all other atoms are free to displace.

Atom	WP		PBEsol	Experiment[29]
Na(2)	4*e*	*x*	0.510	0.509
		y	0.058	0.055
		z	0.750	0.750
F(1)	4*e*	*x*	0.122	0.115
		y	-0.063	-0.058
		z	0.761	0.767
F(2)	4*e*	*x*	0.722	0.719
		y	0.828	0.829
		z	-0.058	-0.053
F(3)	4*e*	*x*	0.162	0.163
		y	0.724	0.721
		z	0.068	0.067
a			5.472	5.471
b			5.684	5.683
c			8.075	8.073

To understand the complex atomic distortions in the monoclinic phase, we first recognize that a group–subgroup relationship exists between the ideal high-symmetry cubic structure without octahedral distortions or rotations, $Fm\bar{3}m$, and the $P2_1/n$ structure.[47] Mode crystallographic analyses[48,49] then enable us to determine the full set of unique symmetry-adapted mode displacements active in the $Fm\bar{3}m \rightarrow P2_1/n$ transition (see Fig. 3 for schematic illustrations), described as irreducible representation (irreps) of $Fm\bar{3}m$. We find that the cubic-to-monoclinic symmetry reduction requires a combination of at least two of these modes; based on the physical character (Fig. 3) and mode amplitudes (Table II) of the distortions appearing in the ground state structure, we deduce that the symmetry reduction is driven by out-of-phase octahedral rotations about the b axis and in-phase rotations about c-axis, *i.e.*, the combination of $\Gamma_4^+ \oplus X_3^+$.

Given that the irreps form a complete basis for which to perform the structure decomposition of the monoclinic phase relative to the cubic structure, we can use the mode amplitude to make a quantitative comparison of the internal atomic positions obtained from our relaxed PBEsol simulation and the experimental structure. Table II reveals that there is only a modest difference (<10% error) between the PBEsol structure and experiment for all mode distortions that are not characterized by distortions of the Jahn-Teller type (Γ_3^+, X_2^+). For example, our

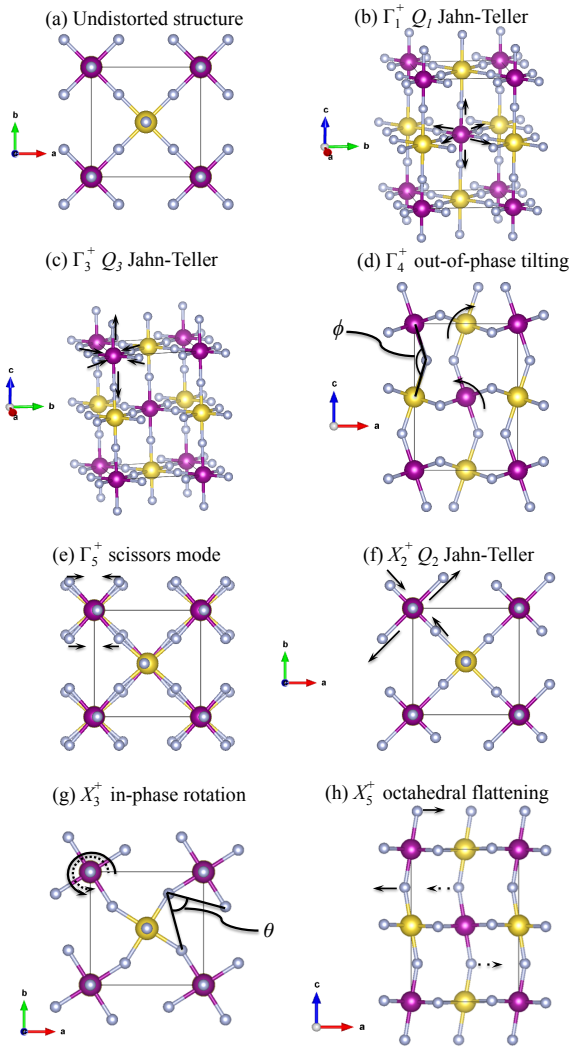

FIG. 3. Illustration of symmetry-adapted mode displacements which appear in monoclinic Na_3MnF_6 labeled according to irreps of the undistorted (a) $Fm\bar{3}m$ structure: (b) Γ_1^+: the Q_1 Jahn-Teller (JT) mode commonly referred to as the breathing distortion. (c) Γ_3^+: the Q_3 (two out–four in) JT vibrational mode. (d) Γ_4^+: the out-of-phase tilting of octahedra about the b axis. The tilt angle is measured as $(180° - \phi)/2$. (e) Γ_5^+: "scissor" mode which brings equatorial F anions in the MnF_6 octahedra closer together and reducing the intra-octahedral F–Mn–F bond angle from the ideal 90°. (f) X_2^+: the Q_2 (two in–two out) bond stretching mode in the ab plane. (g) X_3^+: in-phase rotations of the octahedra about the c axis. The rotation angle is measured as $(90° - \theta)/2$. (h) X_5^+: anti-parallel apical F displacements which lead to a flattening of the MnF_6 octahedra. Note that the Na(2) cations are excluded for clarity throughout, and broken lines indicate atomic displacements in the layer below.

PBEsol calculation underestimate the experimental rotation angle (12.5°) by 3.3%, whereas the experimental tilt angle (19.4°) is overestimated by 5.7%. Both values are within the expected error of 20% for perovskite systems with $a^-a^-c^+$ tilt patterns as predicted with semi-local exchange correlation functionals.[50]

TABLE II. Symmetry-adapted mode amplitudes (in Å) present in the equilibrium Na_3MnF_6 $[P2_1/n]_1$ phase obtained from DFT-PBEsol calculations compared to experiment.[29] The mode amplitudes are normalized with respect to the parent $Fm\bar{3}m$ structure.

Mode	Space group (number)	DFT-PBEsol	Experiment
Γ_1^+	$Fm\bar{3}m$ (225)	0.154	0.175
Γ_3^+	$I4/mmm$ (139)	0.160	0.083
Γ_4^+	$C2/m$ (12)	1.421	1.351
Γ_5^+	$C2/m$ (12)	0.087	0.087
X_2^+	$P4_2/mnm$ (136)	0.056	0.038
X_3^+	$P4/mnc$ (128)	0.892	0.916
X_5^+	$Pnnm$ (58)	0.696	0.656

In the case of JT modes, we find that PBEsol is less accurate in predicting the distortion amplitudes. Specifically, we find a modest 12% underestimation for the Q_1 mode [Fig. 3(b)], but large overestimations of 47% and 92% for the Q_2 and Q_3 modes [Fig. 3(f) and (c)], respectively. Closer inspection of the MnF_6 octahedra shows that these overestimations only manifest as small changes in Mn-F bond lengths of order 10^{-2} Å. (Table III). Our calculations find that the long Mn–F(1) bond is enhanced, while the medium length Mn–F(3) bond is shortened relative to experiment. There is a negligible difference in the short Mn–F(2) bond in the MnF_6 octahedra.

The Jahn-Teller bond length discrepancies found when comparing the DFT predicted values to experiment are common for GGA-level exchange-correlation functionals, and are usually corrected by employing the plus Hubbard U correction.[51–53] Indeed, for Na_3MnF_6 we obtain small improvements in the Jahn-Teller bond distortions with the Hubbard $+U$ correction[54] (data not shown), however this is accompanied by a decrease in the accuracy of the unit cell volume, which should be well-reproduced in order to accurately evolve the system under pressure. Despite the discrepancies, the trend in the Jahn-Teller bond distortions obtained at the PBEsol level are in good agreement with the experimental bond lengths, *i.e.*, Mn–F(1)>Mn–F(3)>Mn–F(2). Thus, we find that the PBEsol functional without the Hubbard correction is a suitable exchange-correlation functional to use to explore the origin of the pressure-induced isosymmetric transition.

TABLE III. Comparison of the Mn–F bond lengths for the ground state Na_3MnF_6 $[P2_1/n]_1$ structure computed with the PBEsol functional to experiment.[29] All units in Å.

Bond	DFT-PBEsol	Experiment
Mn-F(1)	2.084	2.017
Mn-F(2)	1.863	1.862
Mn-F(3)	1.876	1.897

B. Hydrostatic Pressure-induced Isosymmetric Transition

We investigate phase stability of the monoclinic Na_3MnF_6 by computing the total energy at various volumes for both the $[P2_1/n]_1$ and $[P2_1/n]_2$ structures.[55] Fig. 4 shows that the energy of both monoclinic phases increase with increasing pressure (decreasing cell volume). At low-pressure $[P2_1/n]_1$, exhibiting the Jahn-Teller bond axis oriented along the c axis, is more stable than $[P2_1/n]_2$ (JT bond axis in the ab plane) by ∼20 meV. This energetic stability persists until near a unit cell volume of 240 Å, where we find that both monoclinic structures are stable within our simulations. Upon further increase in pressure, $[P2_1/n]_2$ is stabilized relative to $[P2_1/n]_1$ by nearly the same energetic difference. We observe no change in space group symmetry or occupied Wyckoff positions for all volumes computed, consistent with available experimental results, which makes this transition isosymmetric.

We now explore changes in the internal atomic positions with pressure, focusing on the cooperative behavior of the Mn–F octahedra. We first examine the changes in the Mn–F bond lengths. Rather than using the symmetry-mode description described before, we parameterize the structural distortions to the MnF_6 octahedra in terms of first-order Jahn-Teller (JT) elongations Q_2 and Q_3.[56] This allows us to describe the JT modes by the position of the surrounding ligands in an octahedral field whose normal coordinates are associated with the vibrational mode that leads to a crystalline field removing the orbital

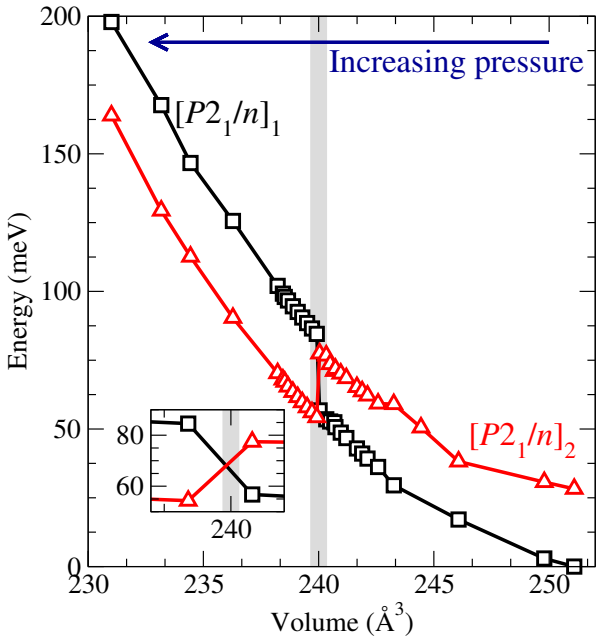

FIG. 4. Evolution of the total energy for the unique monoclinic $[P2_1/n]_1$ and $[P2_1/n]_2$ structures with cell volume given relative to the relaxed zero kelvin $[P2_1/n]_1$ ground state structure. The shaded region highlights the pressure domain of phase coexistence and the transition point about which the stability of the monoclinic phases reverses.

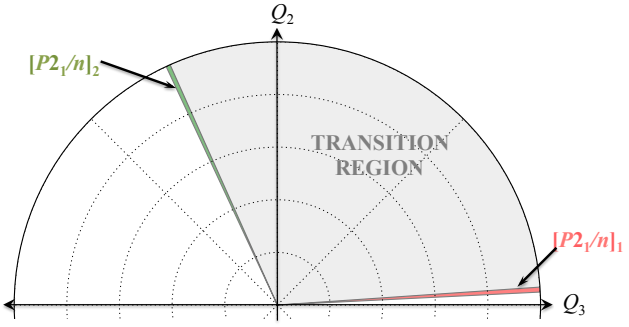

FIG. 5. Phase stability of $[P2_1/n]_1$ and $[P2_1/n]_2$ represented in the $Q_2 - Q_3$ plane of the Jahn-Teller lattice distortions. The red, green, and gray wedges illustrate the stability regions for $[P2_1/n]_1$, $[P2_1/n]_2$, and the transition region, revealing each structure is characterized by a dominant Q_2 or Q_3 mode.

degeneracy. The Q_2 mode is a tetragonal "two-in and two-out" bond distortion in the ab plane [$Q_2 > 0$, Fig. 3(c)], while Q_3 is a three-dimensional "two-out and four-in" bond distortion [$Q_3 > 0$, Fig. 3(f)]. In Na_3MnF_6, the Q_2 and Q_3 vibrational modes are ferrodistortively aligned. In the monoclinic systems studied here, the $Q_2 > 0$ mode elongates the Mn–F bonds that lie mainly along the b axis and shortens those along a, while $Q_3 > 0$ shortens the Mn–F bonds in the ab plane while elongating the bonds along c axis.

We obtain the fraction of the Q_2 and Q_3 JT modes present in the stable monoclinic low- and high-pressure variants as a function of hydrostatic pressure by computing the magnitude of the Jahn-Teller normal modes as follows:

$$Q_2 = \frac{2}{\sqrt{2}}[\mathrm{F}(3) - \mathrm{F}(2)],$$
$$Q_3 = \frac{2}{\sqrt{6}}[2\mathrm{F}(1) - F(2) - \mathrm{F}(3)],$$

where, F(1), F(2), and F(3) are the Mn–F bond lengths directed along the c, a, and b axes, respectively. The JT phase is defined by $\Theta = \tan^{-1} Q_2/Q_3$. Within this formalism, $\Theta = 0°$ represents a JT distortion of octahedra stretched along the c axis. Angles of $\Theta = \pm 120°$ correspond to JT distortions along the b and a axis, respectively.[39,40,57]

Fig. 5 shows the stability of the monoclinic Na_3MnF_6 structures in the Q_2-Q_3 plane with respect to Θ. For $[P2_1/n]_1$, $\Theta = 2.99°$ at ambient pressure and evolves to a maximum of value of 4.06° at the critical pressure. Thus in the low pressure Na_3MnF_6 phase, the Q_3 JT mode dominates the Q_2 mode, leading to a tetragonal distortion of the MnF_6 octahedra that also elongates the c axis and contracts the crystal in the ab plane. Across the IPT there are no intermediate values of Θ (grayed region). In the high pressure phase $[P2_1/n]_2$, a drastic increase in the value of Θ occurs, *i.e.*, $\Theta = 114.1°$ and reaches a maximum of $\Theta = 115.0°$, which indicates a

first order transition to a Q_2-type JT distortion and is consistent with the long bond becoming the Mn–F(3) bond as observed in the $[P2_1/n]_2$ phase.

C. Jahn-Teller Electronic Effects

We now investigate the electronic structure evolution across the IPT to understand the coupling between the electron and lattice degrees of freedom in Na_3MnF_6. Here, Mn(III) is found in a high-spin d^4 configuration with one electron in the e_g manifold, which appears as a strong Jahn-Teller distortion in the octahedra. By definition the first-order Jahn-Teller (FOJT) effect of a transition metal cation in an octahedrally coordinated field acts to remove the electronic degeneracy of unevenly occupied t_{2g} (weak JT) or e_g (strong JT) orbitals by inducing a structural distortion.[58–60] Thus, we anticipate that hydrostatic pressure directly affects the value of Θ in the Q_2-Q_3 subspace.

Importantly, the value of Θ also provides a measure of the average character of the occupied molecular orbital state $|\Theta\rangle$ of the Jahn-Teller ion for a given static cooperative JT distortion as an arbitrary superposition of the e_g orbitals wave functions.[39,61] It can be approximated for a system at absolute zero as[57]

$$|\Theta\rangle = \cos(\Theta/2)\,|d_{z^2-r^2}\rangle + \sin(\Theta/2)\,\left|d_{x^2-y^2}\right\rangle .$$

We use Maximally Localized Wannier Functions (MLWF)[62,63] to transform our periodic wave functions forming the valence band (VB) and conduction band (CB) edges into a local real-space representation of the e_g ($d_{x^2-y^2}$ and $d_{z^2-r^2}$) orbitals. The subspace is spanned by these atomic-like orbitals for the two Mn cations in the unit cell to evaluate the percent character of each orbital contributing to $|\Theta\rangle$.

Fig. 6(a) shows the electronic band structure near the Fermi level (E_F) for $[P2_1/n]_1$ at ambient pressure. The occupied bands are largely $3d_{z^2-r^2}$-like Mn states while the $3d_{x^2-y^2}$ orbital forms the conduction band throughout the Brillouin zone (BZ). It is significant to note that $\Theta = 2.99°$ for $[P2_1/n]_1$ at ambient pressure and this corresponds to $|\Theta\rangle$ being comprised of 99.9% $d_{z^2-r^2}$ orbital character in agreement with the MLWF projection Fig. 6(a). This result is characteristic of the orbital splitting anticipated for $Q_3 > 0$, where the apical bonds in the MnF_6 octahedra are elongated and the equatorial bonds contract.[40] The MLWFs reveal strong localization of the atomic like $3d_{z^2-r^2}$ orbital on the Mn cations below E_F [Fig. 6(c)]; the majority spin $e_g^{\uparrow}$ electron occupies the orbital directed along the long JT-bond to reduce the Coulombic repulsion induced by the F $2p$ electron cloud.

Fig. 6(b) depicts the electronic structure for $[P2_1/n]_2$ at 2.50 GPa. From the projection onto the MLWFs, we observe in the high pressure phase that the VB and CB adopt mixed e_g-orbital character throughout the BZ. The occupied orbital, although dominated by atomic $d_{x^2-y^2}$ character, has an admixture of $d_{z^2-r^2}$ [Fig. 6(d)]. At

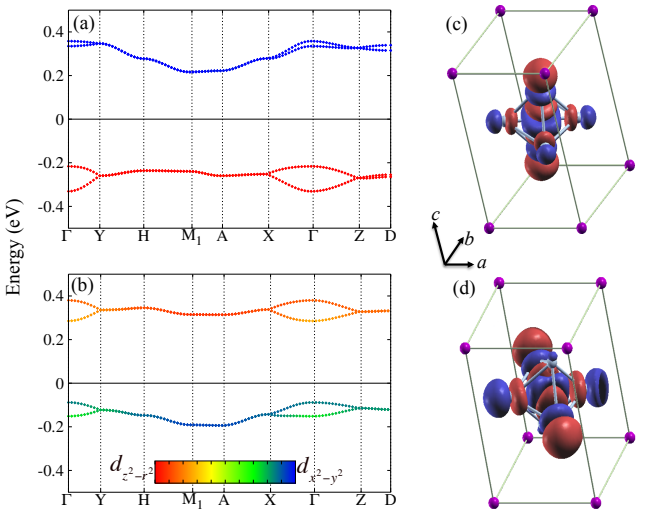

FIG. 6. Low energy electronic band structure about the Fermi level (horizontal line at 0 eV) with the projected e_g orbital character for Na_3MnF_6 at (a) $[P2_1/n]_1$ (0.0 GPa), and (b) $[P2_1/n]_2$ (2.5 GPa). The maximally-localized Wannier Functions (MLWF) for the occupied molecular orbital for the (c) $[P2_1/n]_1$ and (d) $[P2_1/n]_2$.

2.50 GPa $\Theta = 114.2°$ in $[P2_1/n]_2$, and this angle predicts a wavefunction with 29.5% $d_{z^2-r^2}$ orbital character. The mixed e_g molecular orbital state is typical for manganates with a Q_2-like JT distortion, *i.e.*, the long-JT bond axis is oriented in the ab plane.[40,64,65]

We now examine the energetics associated with the changes in $|\Theta\rangle$ by computing the $Q_2 - Q_3$ energy surface using the calculated total energies of $[P2_1/n]_1$ and $[P2_1/n]_2$ and fitting to a Taylor series expansion (Fig. 7). We achieve this by incrementally increasing the Q_2 (X_2^+) and Q_3 (Γ_3^+) symmetry-adapted mode amplitudes in the $[P2_1/n]_1$ phase at ambient pressure (Table II) and $[P2_1/n]_2$ at 2.50 GPa (Table IV) with respect to the undistorted reference structures.[66] In Fig. 7, mode amplitudes of $Q_2 > 0$ represent a JT distortion which elongates the Mn–F(3) bond and shortens the Mn–F(2) bonds in the ab plane, while $Q_2 < 0$ shortens Mn–F(3) and elongates Mn–F(2). Similarly, $Q_3 > 0$ mode amplitudes correspond

TABLE IV. Symmetry-adapted mode amplitudes (in Å) present in the Na_3MnF_6 $[P2_1/n]_2$ phase at 2.50 GPa obtained from DFT-PBEsol calculations. The mode amplitudes are normalized with respect to the parent $Fm\bar{3}m$ structure.

Mode	Space group (number)	DFT-PBEsol
Γ_1^+	$Fm\bar{3}m$ (225)	0.119
Γ_3^+	$I4/mmm$ (139)	0.103
Γ_4^+	$C2/m$ (12)	1.465
Γ_5^+	$C2/m$ (12)	0.219
X_2^+	$P4_2/mnm$ (136)	0.083
X_3^+	$P4/mnc$ (128)	0.892
X_5^+	$Pnnm$ (58)	0.786

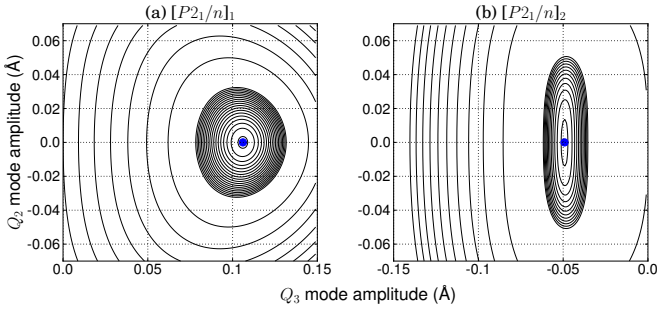

FIG. 7. Calculated two-dimensional energy surface contours for (a) $[P2_1/n]_1$ at ambient pressure and (b) $[P2_1/n]_2$ at 2.50 GPa with respect to the amplitude of the Q_2 and Q_3 JT modes derived from mode crystallography. The filled (blue) circles denote the position of minima in the potential energy surface.

to a two-out–four-in JT distortion which stretches the apical Mn–F(1) while shortening the Mn–F(2) and Mn–F(3) equatorial bonds. Conversely, $Q_3 < 0$ gives the four-out–two-in JT bonding environment that elongates bonds in the *ab* plane [Mn–F(2) and Mn–F(3)] and shortens the Mn–F(1) bond.

Considering only JT modes in the equilibrium volume of $[P2_1/n]_1$ at ambient pressure, we find a single energy minimum at $Q_3 \sim 0.11$ and $Q_2 = 0$ [Fig. 7(a)]. In this phase, a two-out–four-in Q_3 JT vibrational mode stabilizes Na_3MnF_6 at ambient pressure by approximately 38.6 meV/f.u. over the undistorted phase, which is consistent with the structural and electronic investigations already described. Despite having a small finite amplitude of Q_2 (X_2^+) present in the equilibrium structure [Table II], Fig. 7(a) indicates that in the absence of other distortions any nonzero amplitude of Q_2 leads to an energetic penalty in $[P2_1/n]_1$. Thus, an asymmetrical Mn–F bond stretching in the *ab* plane is an unfavorable distortion at ambient conditions without the presence of another distortion.

From Fig. 7(b), we observe that our two-dimensional energy surface predicts a single energy minimum for $[P2_1/n]_2$ at 2.50 GPa. Here, the minimum is located at $Q_3 \sim -0.048$ and $Q_2 = 0$. In the stable $[P2_1/n]_2$ phase, it is noteworthy that the stability regime for the Q_3 vibrational mode is in a negative range. This indicates that unlike the $[P2_1/n]_1$ phase, at elevated pressures across the IPT a four-out–two-in Q_3 rather than two-out–four-in Mn–F distortion is required to stabilize the structure. According to the JT theory, a d^4 cation with $Q_3 < 0$ distortion splits the e_g degeneracy by occupying the $d_{x^2-y^2}$ orbital. Thus, the change in sign of the Q_3 mode is in accord with the $d_{x^2-y^2}$ dominate valence band edge observed in our electronic structure calculations (Fig. 6). However, since $Q_2 = 0$ in the absence of any other distortion, at high pressure Na_3MnF_6 would exhibit four equivalent equatorial bonds, *i.e.*, Mn–F(2) = Mn–F(3), in the reduced subspace. The latter is in contrast to the fully relaxed atomic and electronic structure of the $[P2_1/n]_2$ phase, where the MnF_6 octahedra exhibit multiple distortions with an approximately $Q_2 > 0$-like JT bonding

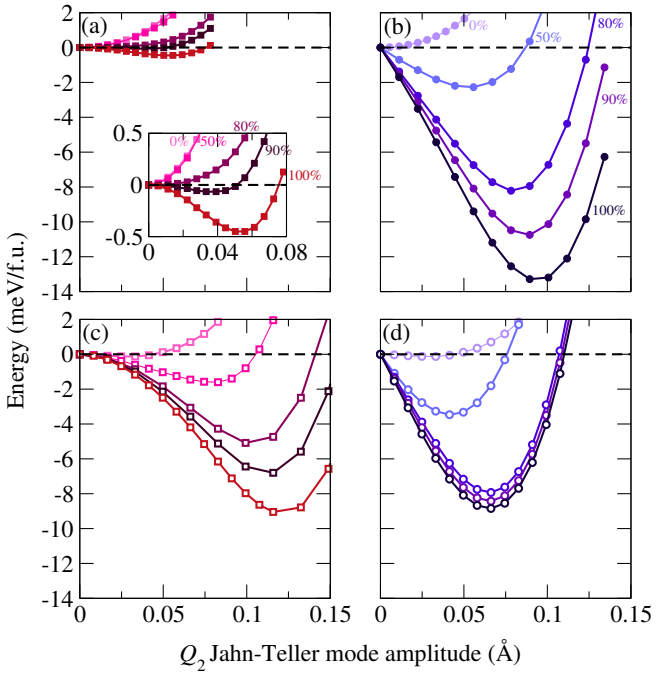

FIG. 8. Energy evolution from the coupling of the Q_2 Jahn-Teller distortion to the tilt and rotation at (a) and (b) ambient pressure (filled symbols) and at (c) and (d) 2.50 GPa (unfilled symbols), respectively. Normalized energy gain obtained by increasing the amplitude of Q_2 at fixed percentages of the out-of-phase tilt found in the ground equilibrium structures.

environment. Indeed, the symmetry-adapted mode amplitudes for Na_3MnF_6 at 2.50 GPa (Table IV) indicate that the Q_2 mode (X_2^+) is finite and larger in amplitude ($Q_2 = 0.083$) than at ambient pressure ($Q_2 = 0.056$).

We now seek to identify which other structural distortion (non-Jahn-Teller mode) acts to stabilize nonzero Q_2 mode amplitudes in the equilibrium structures. From the mode decomposition analysis at ambient and elevated pressure, we observe that the largest contribution to the equilibrium structures arise from the tilt (Γ_4^+) and rotation (X_3^+) of the MnF_6 units. To understand the nature of the tilt–Q_2 and rotation–Q_2 coupling, we incrementally increase the mode amplitude of Q_2 at finite amplitudes of the tilt and rotation (0%, 50%, 80%, 90% and 100% of their maximum) with respect to the undistorted reference structure.

Fig. 8 shows that both the tilt and rotation modes couple to Q_2 and give a net energy gain in the free energy in both pressure regimes at finite amplitude. From Fig. 8(a) we observe that as the amplitude of tilt irrep increases in $[P2_1/n]_1$, the curvature of the Q_2 free energy evolves from a positive parabola with a single minimum at the $Q_2 = 0$ to a double-well potential with negative curvature about the origin and minima at finite Q_2 for tilt amplitudes $\geq 80\%$. This signifies a continuous softening of the Q_2 phonon mode induced by large amplitudes of the tilt mode (Γ_4^+ irrep), which effectively stabilizes the finite asymmetrical stretching observed in the ground state (Table II)

through a fourth-order biquadratic anharmonic interaction that renormalizes the mode stiffness of the quadratic Q_2^2 mode. The behavior of the MnF_6 rotation–Q_2 coupling in Fig. 8(b) shows that there is a large energetic gain associated with increasing amplitudes of the rotation mode. The single minima of the parabolic energy curves indicate, however, that while this coupling contributes to the total energy it does not soften the Q_2 mode frequency, but rather shifts the mode amplitude of Q_2 to a non-zero value through a linear-quadratic interaction.

In the high pressure phase (2.50 GPa) [Fig. 8(c) and (d)], we observe that the Q_2 irrep is unstable with a small energy gain < 1 meV at 0% tilt and rotation amplitudes. Fig. 8(c) shows that increasing the amplitude of the tilt distortion in the $[P2_1/n]_2$ leads to an enhanced energy stabilization, which ultimately promotes a larger Q_2 distortion in the high pressure phase. In contrast, increasing the contribution of the rotational mode hardens the Q_2 mode [Fig. 8(d)], thereby reducing the energetic gain and leading to a smaller amplitude of Q_2 through the coupled $Q_2^2 Q_{X_3^+}$ interaction.

IV. DISCUSSION

Our calculations and structural analysis indicate that the IPT is due to the spontaneous redistribution of the electronic charge density among the e_g orbitals of the strong JT Mn cation. Specifically, we find that the low pressure system is stabilized with the long bond along the c axis and a filled $d_{z^2-r^2}$ orbital which is characteristic of a $Q_3 > 0$ JT where $c/a > 1$.[39,40] Mode crystallographic analyses coupled with phenomenological Landau investigations of the JT Mn–F bond distortions reveal that the lattice strain induced by hydrostatic pressure renormalizes the mode stiffness of the JT vibrational modes across the transition. The leading coefficient of the Q_3^2 term in the Hamiltonian changes sign under hydrostatic pressure.

Most significantly, we observe that across the transition the Q_3 JT irrep switches from a two-out-four-in ($Q_3 > 0$) in $[P2_1/n]_1$ to a four-out-two-in ($Q_3 < 0$) in the $[P2_1/n]_2$ phase. While the key structural signature defining $[P2_1/n]_2$ is a Q_2-like Mn–F bonding arrangement, we contend that the primary factor in the stabilization of the high pressure phase in Na_3MnF_6 is the change in sign of the Q_3 distortion mediated by the Q_2–MnF_6 tilt interaction. Table II and Table IV clearly show that the rotation amplitude is unchanged under pressure. Our electronic and phenomenological investigations indicate that at high pressure, it is more favorable for the charge to localize in the $d_{x^2-y^2}$-like orbital. Thus, the characteristic Q_2-like Mn–F_6 bonding distortion that differentiates the $[P2_1/n]_2$ and $[P2_1/n]_1$ phases is stabilized by second-order effects. We show that a strong coupling exists between the tilt and Q_2 lattice degrees of freedom owing to an anharmonic interaction that stabilizes finite amplitudes of Q_2 in the equilibrium structures. The importance of this secondary effect is highlighted by comparing [Fig. 8(a) and (c)], as

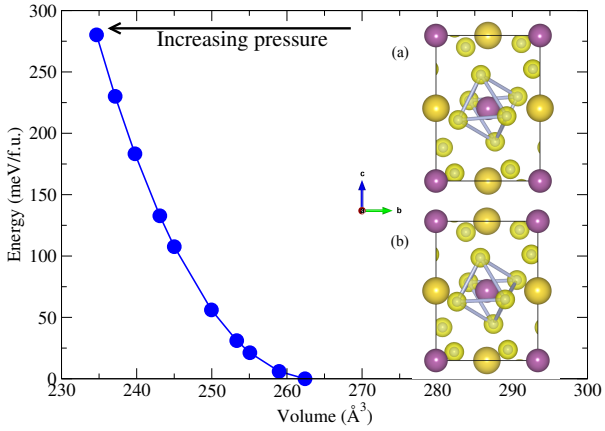

FIG. 9. Evolution of the total energy of Na_3ScF_6 with cell volume relative to the DFT relaxed ground state structure. The inset depicts the partial charge density obtained over the energy window ranging from -2 eV to E_F at (a) ambient pressure (0.0 GPa) and (b) 6.82 GPa. Unlike Na_3MnF_6, neither a structural transition nor charge redistribution is observed.

the energetic gain produced by the tilt–Q_2 coupling increases by approximately 20-fold in the $[P2_1/n]_2$ phase at equilibrium over the ambient case.

In addition, our electronic structure calculations show that hydrostatic pressure has an effect on the crystal field splitting in the stable phases of Na_3MnF_6. We observe that energy gap between the filled $d_{z^2-r^2}$ and the unoccupied $d_{x^2-y^2}$ is reduced from 0.43 eV at ambient pressure to 0.34 eV at the transition. Across the critical pressure for the transition, the band gap is 0.37 eV at 2.20 GPa. The continued application of hydrostatic pressure in the high pressure phase further decreases the band gap at approximately 0.02 eV/GPa which allows us to predict a insulator-to-metal transition around ∼20 GPa.

Based on this understanding, we performed a similar set of calculations for the d^0 compound Na_3ScF_6, which also crystallizes with $P2_1/n$ symmetry and for which experimental structural data under hydrostatic pressure exists.[67] We find there is no discontinuity in either the total energies (Fig. 9) or in the evolution of the Sc–F bond lengths up to a pressure of 6.82 GPa, which indicates that no isosymmetric transitions occur up to a pressure that is approximately 4.7 GPa higher than required for the fluoromanganate. Indeed, Fig. 9 shows the partial charge density for Na_3ScF_6 obtained by integrating over a finite region from -2 eV to E_F is highly uniform at both ambient Fig. 9(a) and high pressure Fig. 9(b). The absence of both a JT instability and an anisotropic bonding environment is consistent with the experimental findings and the proposed electronic origin for the IPT in Na_3MnF_6, highlighting the importance of the JT-active Mn(III).

V. CONCLUSION

We used first principles density functional calculations to study the electronic and atomic origins of the first-order

pressure induced phase transition in Na_3MnF_6. We identified that the isosymmetric transition originates from two key features present in the fluoromangante: (i) a Jahn-Teller active Mn(III) ion with an e_g orbital degeneracy, and (ii) the strong coupling of the cooperative Mn–F bond distortions to MnF_6 octahedral tilts with hydrostatic pressure. We find that while simple structural arguments may identify the $[P2_1/n]_1$ phase of Na_3MnF_6 as being dominated by a Q_3-type JT distortion and the $[P2_1/n]_2$ phase as Q_2-type, the combined effect of both distortions with collective MnF_6 tilts are essential to describing the stability of the structure at both ambient and under hydrostatic pressure. In the $[P2_1/n]_1$ structures the $Q_3 > 0$ JT distortion splits the e_g manifold into atomic-like occupied $d_{z^2-r^2}$ and an unoccupied $d_{x^2-y^2}$ orbitals, owing to an elongated JT Mn–F bond aligned along the crystallographic c-axis. After the transition to the high-pressure phase $[P2_1/n]_2$, the JT-bond axis reorients into the ab plane with the structure largely characterized by a Q_2-type bonding arrangement. The transition above 2.15 GPa is arguably driven by a spontaneous renormalization of the Q_3 vibrational mode, *i.e.*, $Q_3 < 0$. The equilibrium structure of the $[P2_1/n]_2$ phase is stabilized by secondary lattice effects which couple the tilt and Q_2 JT phonon modes to give the Mn–F(3) > Mn–F(1) > Mn–F(2), which is the signature of the high pressure phase of Na_3MnF_6.

ACKNOWLEDGMENTS

N.C. thanks Danilo Puggioni for useful discussions. N.C. and J.M.R. acknowledge the donors of The American Chemical Society Petroleum Research Fund for support (Grant No. 52138-DNI10). DFT calculation were performed on the high-performance computing facilities available at the Center for Nanoscale Materials (CARBON Cluster) at Argonne National Laboratory, supported by the U.S. DOE, Office of Basic Energy Sciences (BES), DE-AC02-06CH11357.

* neniancharles@drexel.edu
† jrondinelli@coe.drexel.edu

[1] R. A. F. Pinlac, C. L. Stern, and K. R. Poeppelmeier, Crystals **1**, 3 (2011).
[2] A. T. Mulder, N. A. Benedek, J. M. Rondinelli, and C. J. Fennie, Advanced Functional Materials **23**, 4810 (2013).
[3] L. Qiao, K. H. L. Zhang, M. E. Bowden, T. Varga, V. Shutthanandan, R. Colby, Y. Du, B. Kabius, P. V. Sushko, M. D. Biegalski, and S. A. Chambers, Advanced Functional Materials **23**, 2953 (2013).
[4] L. Martin and R. Ramesh, Acta Materialia **60**, 2449 (2012).
[5] J. M. Rondinelli, S. J. May, and J. W. Freeland, MRS Bulletin **37**, 261 (2012).
[6] M. Imada, A. Fujimori, and Y. Tokura, Reviews of Modern Physics **70**, 1039 (1998).
[7] J. B. Goodenough, Chemistry of Materials **26**, 820 (2014).
[8] D. G. Schlom, L.-Q. Chen, X. Pan, A. Schmehl, and M. A. Zurbuchen, J. Amer. Ceram. Soc. **91**, 2429 (2008).
[9] L. W. Martin, S. P. Crane, Y.-H. Chu, M. B. Holcomb, M. Gajek, M. Huijben, C.-H. Yang, N. Balke, and R. Ramesh, Journal of Physics: Condensed Matter **20**, 434220 (2008).
[10] V. M. Goldschmidt, Naturwissenschaften **14**, 477 (1926).
[11] M. T. Anderson, K. B. Greenwood, G. A. Taylor, and K. R. Poeppelmeier, Progress in Solid State Chemistry **22**, 197 (1993).
[12] G. King and P. M. Woodward, J. Mater. Chem. **20**, 5785 (2010).
[13] T. Saha-Dasgupta, Journal of Physics: Condensed Matter **26**, 193201 (2014).
[14] J. Young and J. M. Rondinelli, Chemistry of Materials **25**, 4545 (2013).
[15] O. Erten, O. N. Meetei, A. Mukherjee, M. Randeria, N. Trivedi, and P. Woodward, Phys. Rev. Lett. **107**, 257201 (2011).
[16] D. D. Sarma, P. Mahadevan, T. Saha-Dasgupta, S. Ray, and A. Kumar, Phys. Rev. Lett. **85**, 2549 (2000).
[17] O. N. Meetei, O. Erten, M. Randeria, N. Trivedi, and P. Woodward, Phys. Rev. Lett. **110**, 087203 (2013).
[18] J. Ravez, J. Phys. III France **7**, 1129 (1997).
[19] C. Ederer and N. A. Spaldin, Phys. Rev. B **74**, 020401 (2006).
[20] J. F. Scott and R. Blinc, Journal of Physics: Condensed Matter **23**, 113202 (2011).
[21] A. C. Garcia-Castro, N. A. Spaldin, A. H. Romero, and E. Bousquet, Phys. Rev. B **89**, 104107 (2014).
[22] F. C. Hawthorne and R. B. Ferguson, The Canadian Mineralogist **13**, 377 (1975).
[23] L. R. Moras, Journal of Inorganic and Nuclear Chemistry **36**, 3876 (1974).
[24] I. Flerov, M. Gorev, K. Aleksandrov, A. Tressaud, J. Grannec, and M. Couzi, Materials Science and Engineering: R: Reports **24**, 81 (1998).
[25] W. Massa and D. Babel, Chemical Reviews **88**, 275 (1988).
[26] R. D. Shannon and C. T. Prewitt, Acta Crystallographica Section B **26**, 1046 (1970).
[27] R. D. Shannon, Acta Crystallographica Section A **32**, 751 (1976).
[28] R. L. Cook and A. F. Sammells, Solid State Ionics **45**, 311 (1991).
[29] U. Englich, W. Massa, and A. Tressaud, Acta Crystallographica Section C **48**, 6 (1992).
[30] S. Carlson, Y. Xu, U. Hlenius, and R. Norrestam, Inorganic Chemistry **37**, 1486 (1998).
[31] J. F. Scott, Advanced Materials **22**, 2106 (2010).
[32] J. M. Rondinelli and S. Coh, Physical Review Letters **106**, 235502 (2011).
[33] A. G. Christy, Acta Crystallographica Section B **51**, 753 (1995).
[34] A. S. Gibbs, K. S. Knight, and P. Lightfoot, Phys. Rev. B **83**, 094111 (2011).
[35] Z. Chen, Z. Luo, C. Huang, Y. Qi, P. Yang, L. You, C. Hu, T. Wu, J. Wang, C. Gao, T. Sritharan, and L. Chen, Advanced Functional Materials **21**, 133 (2011).

[36] H. M. Christen, J. H. Nam, H. S. Kim, A. J. Hatt, and N. A. Spaldin, Phys. Rev. B **83**, 144107 (2011).
[37] G. Gou and J. M. Rondinelli, Advanced Materials Interfaces (2014), 10.1002/admi.201400042.
[38] A. J. Hatt, N. A. Spaldin, and C. Ederer, Phys. Rev. B **81**, 054109 (2010).
[39] K. I. Kugel and D. I. Khomski, Soviet Physics Uspekhi **25**, 231 (1982).
[40] J. B. Goodenough, A. Wold, R. J. Arnott, and N. Menyuk, Phys. Rev. **124**, 373 (1961).
[41] J. P. Perdew, A. Ruzsinszky, G. I. Csonka, O. A. Vydrov, G. E. Scuseria, L. A. Constantin, X. Zhou, and K. Burke, Phys. Rev. Lett. **100**, 136406 (2008).
[42] G. Kresse and J. Furthmüller, Phys. Rev. B **54**, 11169 (1996).
[43] G. Kresse and D. Joubert, Phys. Rev. B **59**, 1758 (1999).
[44] P. E. Blöchl, Phys. Rev. B **50**, 17953 (1994).
[45] H. J. Monkhorst and J. D. Pack, Physical Review B **13**, 5188 (1976).
[46] A. M. Glazer, Acta Crystallographica Section B **28**, 3384 (1972).
[47] The occupied Wyckoff sites for Na_3MnF_6 in the $Fm\bar{3}m$ space group are 4*a* for Mn, 4*b* for Na(1), 8*c* for Na(2), and 24*e* for F.
[48] B. J. Campbell, H. T. Stokes, D. E. Tanner, and D. M. Hatch, Journal of Applied Crystallography **39**, 607 (2006).
[49] J. M. Perez-Mato, D. Orobengoa, and M. I. Aroyo, Acta Crystallographica Section A **66**, 558 (2010).
[50] P. Garcia-Fernandez, S. Ghosh, N. J. English, and J. A. Aramburu, Phys. Rev. B **86**, 144107 (2012).
[51] H. Sawada, Y. Morikawa, K. Terakura, and N. Hamada, Phys. Rev. B **56**, 12154 (1997).
[52] I. Leonov, D. Korotin, N. Binggeli, V. I. Anisimov, and D. Vollhardt, Phys. Rev. B **81**, 075109 (2010).
[53] J. H. Lee, K. T. Delaney, E. Bousquet, N. A. Spaldin, and K. M. Rabe, Phys. Rev. B **88**, 174426 (2013).
[54] S. L. Dudarev, L.-M. Peng, S. Y. Savrasov, and J.-M. Zuo, Physical Review B **61**, 2506 (2000).
[55] Fine sampling near the reported[30] transition pressure is achieved by extrapolating best fit lines of the evolution of lattice parameters from the energetically more stable $[P2_1/n]_2$.
[56] J. H. Van Vleck, The Journal of Chemical Physics **7**, 72 (1939).
[57] J. Kanamori, Journal of Applied Physics **31**, S14 (1960).
[58] M. A. Carpenter and C. J. Howard, Acta Crystallographica Section B **65**, 134 (2009).
[59] J. B. Goodenough, Reports on Progress in Physics **67**, 1915 (2004).
[60] J. B. Goodenough, Annual Review of Materials Science **28**, 1 (1998).
[61] A. Stroppa, P. Barone, P. Jain, J. M. Perez-Mato, and S. Picozzi, Advanced Materials **25**, 2284 (2013).
[62] N. Marzari and D. Vanderbilt, Phys. Rev. B **56**, 12847 (1997).
[63] A. A. Mostofi, J. R. Yates, Y.-S. Lee, I. Souza, D. Vanderbilt, and N. Marzari, Computer Physics Communications **178**, 685 (2008).
[64] J. E. Medvedeva, M. A. Korotin, V. I. Anisimov, and A. J. Freeman, Phys. Rev. B **65**, 172413 (2002).
[65] Y. Murakami, J. P. Hill, D. Gibbs, M. Blume, I. Koyama, M. Tanaka, H. Kawata, T. Arima, Y. Tokura, K. Hirota, and Y. Endoh, Phys. Rev. Lett. **81**, 582 (1998).
[66] The undistorted structures are constructed to have cell volumes and monoclinic angles that correspond to the pressure being studied with all mode amplitudes equal to zero relative to the DFT-PBEsol relaxed monoclinic structures. The energy maps are obtained from 225 self-consistent total energy calculations and then fitting these points to a polynomial expansion in orders of Q_2 and Q_3.
[67] S. Carlson, Y. Xu, and R. Norrestam, Journal of Solid State Chemistry **135**, 116 (1998).